PAPER

Check for updates

Engineering $NiCo_2S_4$ nanoparticles anchored on carbon nanotubes as superior energy-storage materials for supercapacitors†

Junming Chen,‡[ab] Zhiling Du,‡[c] Kun Cheng,[ab] Jusheng Bao,[ab] Guiling Wang,[ab] Yue Yao,[ab] Jiayi Song,[ab] Jing Yue,[ab] Kun Xu,[ab] Weicheng Xie,[ab] Wei Qiang,[ab] You Liu ID *[ab] and Xuchun Wang*[ab]

Fabricating high-capacity electrode materials toward supercapacitors has attracted increasing attention. Here we report a three-dimensional $CNTs/NiCo_2S_4$ nanocomposite material synthesized successfully by a facile one-step hydrothermal technique. As expected, a $CNTs/NiCo_2S_4$ electrode shows remarkable capacitive properties with a high specific capacitance of 890 C g^{-1} at 1 A g^{-1}. It also demonstrates excellent cycle stability with an 83.5% capacitance retention rate after 5000 cycles at 10 A g^{-1}. Importantly, when assembled into a asymmetric supercapacitor, it exhibits a high energy density (43.3 W h kg^{-1}) and power density (800 W kg^{-1}). The exceptional electrochemical capacity is attributed to the structural features, refined grains, and enhanced conductivity. The above results indicate that $CNTs/NiCo_2S_4$ composite electrode materials have great potential application in energy-storage devices.

1. Introduction

Environmental pollution and resource shortages have heightened awareness of the importance of clean and renewable energy.[1–3] Compared with secondary batteries, supercapacitors, a kind of promising energy storage device, have lots of advantages, such as environmental friendliness, low cost, superior safety, high power density and outstanding cycle life, and so they are considered as reliable substitutes for traditional batteries and capacitors.[4,5] Additionally, supercapacitors possess significant application potential in regenerative braking techniques, burst mode power output devices, and short-term energy storage equipment.[6–8] Generally, the charge-storage in supercapacitors mainly involve two means, namely electrical double-layer capacitors (EDLCs) and pseudocapacitors (PCs).[9–11] It is known that EDLCs have rapid charge–discharge capability, but the low energy density due to the limited charge storage only depending on the electrostatic

charge accumulation between electrodes and electrolytes greatly restricts their wide-ranging application.[12–14] PCs can contribute to higher charge-storage density than EDLCs by electrochemical redox reaction of the electrode materials, while low conductivity and structural degradation stimulate the exploration of new PC electrode materials.[15–17]

Currently, transition metal oxides (MnO_2 and Co_3O_4) and transition metal sulfides ($NiCo_2S_4$) are regarded as popular pseudocapacitor electrode materials,[18–20] and the conductivity of metal sulfides is better than that of metal oxides. In recent years, various works are reported about nickel–cobalt layered double hydroxide, transition metal oxides and sulfides for pseudocapacitors.[21–23] Researches indicate that, compared single-component sulfides, binary metal sulfides have higher specific capacity owing to their more redox reactions.[24,25] Nickel–cobalt sulfide possess the fast Faraday reaction from the synergistic reaction of nickel and cobalt and it is reckoned as a promising candidate with enhanced electrocapacitive property toward energy-storage devices.[26–29] To date, nickel–cobalt sulfides with various nanostructures, including nanowires, nanosheets and nanoparticles, have been extensively studied.[30–32] However, the nanomaterials tend to reunite into agglomeration which leads to low specific surface area and the degradation of electrochemical properties.[33,34]

Importantly, previous reports usually regard CNT as a carbon nanomaterials compounded with $NiCo_2S_4$, focusing more on its low cost, high stability and high conductivity.[35–37] In this work, we developed a straightforward one-step hydrothermal procedure to produce 3D composite structure of $NiCo_2S_4$

[a]College of Chemistry and Materials Engineering, Anhui Science and Technology University, Bengbu, Anhui 233000, China. E-mail: liuyou@ahstu.edu.cn; wangxc@ahstu.edu.cn

[b]Anhui Province Quartz Sand Purification and Photovoltaic Glass Engineering Research Center, Bengbu, Anhui 233000, China

[c]School of Energy and Environmental, Hebei University of Engineering, Handan 056038, China

‡ These authors contributed equally to this work as co-first authors.

nanoparticles anchored on carbon nanotubes (CNTs). With the help of abundant functional groups (–COOH, –OH, *etc.*) on the surfaces of CNTs can coordinate with metal ions with empty d orbitals to form a relatively stable CNT-metal ion coordination composites. The metal nanoparticles are restricted between the CNTs to form ultrafine nanocrystals with stable structures, which effectively prevents the agglomeration and growth of the nanoparticles during the reaction. Reducing the size of nanoparticles can increase the specific surface area and provide more active sites, thereby improving its electrochemical performance.

Here, we designed an approach for manufacturing 3D nickel–cobalt sulfide/carbon nanotubes ($CNTs/NiCo_2S_4$) with a hybrid nanostructure using a straightforward one-step hydrothermal route. SEM and TEM images confirm that $NiCo_2S_4$ nanoparticles are evenly anchored on CNTs in $CNTs/NiCo_2S_4$. The corresponding electrochemical performance characterizations shows that $CNTs/NiCo_2S_4$ composite nanoelectrode presents an outstanding specific capacitance of 890 C g^{-1} at the current density of 1 A g^{-1}, the excellent cycle stability with a high capacitance retention rate of 83.5% after 5000 cycles. Besides, an asymmetric supercapacitor based on $NiCo_2S_4$ as positive electrode exhibit a high energy density of 44.33 W h kg^{-1} and a power density of 800 W kg^{-1}. It is speculated that carbon nanotubes as a conductive support can significantly increase the conductivity of composite and effectively prevent the agglomeration of $NiCo_2S_4$ nanoparticles.

2. Experimental details

2.1. Preparation of $CNTs/NiCo_2S_4$

Fig. 1 depicts the preparation process for $CNTs/NiCo_2S_4$ in detail. Typical mixtures consist of 45 mL of ethylene glycol and 15 mL of deionized water with 872.37 mg nickel(II) nitrate hexahydrate, 1746.18 mg cobaltous(II) nitrate hexahydrate, and 913.44 mg thiourea. Afterwards, stirring produced a clear, uniform solution. Following that, 0.1 g of carbon nanotubes were added to the aforesaid solution and stirred for 1 hour following ultrasonic dispersion. After 12 hours of heating at 180 °C, the solution was placed in an autoclave. A black powder is labeled as $CNTs/NiCo_2S_4$ after being cleaned with deionized water and ethanol. In contrast, $NiCo_2S_4$ was synthesized using the same procedure described above but without the addition of carbon nanotubes.
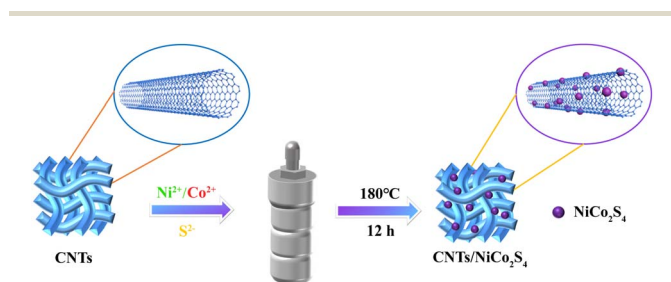

Fig. 1 Schematic depiction of the $CNTs/NiCo_2S_4$ composite preparation.

2.2. Characterization of materials and electrochemical properties

The microstructure of sample was characterized by using a scanning electron microscope (SEM) (JSM-7680F Plus) and a transmission electron microscope (TEM) (JEM-1400 Plus). To study the crystallinity structure of the samples, XRD was used on Smartlab-4. The spectrometer (Thermo ESCALAB 250XI) was used to analyze the elements. By using an inVia reflection spectrometer, we characterized the Raman spectrum of the sample. The conductivity of the material was evaluated using a semiconductor powder resistivity instrument (MCP-PD51).

The electrochemical characterization of the materials were determined by a three-electrode system (Hg/HgO as the reference electrode) on an electrochemical workstation of CHI 660E (Chenhua, Shanghai, China).

3. Results and discussion

The XRD patterns of $NiCo_2S_4$ and $CNTs/NiCo_2S_4$ nanocomposites are displayed in Fig. 2a. It can be seen that the crystal planes of (220), (311), (400), (511) and (440) for the $NiCo_2S_4$ (JCPDS no. 20-0782) are represented by the diffraction peaks at 26.83°, 31.58°, 38.31°, 50.46°, and 55.33°, respectively.[38] The Raman patterns (Fig. 2b) confirm that the pure $NiCo_2S_4$ and $CNTs/NiCo_2S_4$ samples exhibit the same peaks in the 100–800 cm^{-1} range.[39] In addition, the peaks of the $CNTs/NiCo_2S_4$ nanocomposites have obvious D and G peaks, which is consistent with the results of pure CNTs, indicating that the $CNTs/NiCo_2S_4$ nanocomposites are successfully synthesized. Moreover, the electrical conductivity of $CNTs/NiCo_2S_4$ nanocomposites is *ca.* 9.85 S cm^{-1} in Fig. 2c, which is significantly better than that of pure $NiCo_2S_4$ (5.87 S cm^{-1}). The SEM images of $NiCo_2S_4$ and $CNTs/NiCo_2S_4$ samples are shown in Fig. 2d and e, respectively. Pure $NiCo_2S_4$ sample reveals a uniform nanospherical structure with a diameter of *ca.* 500 nm. SEM images of $CNTs/NiCo_2S_4$ composite samples show that the composite consists of CNTs and $NiCo_2S_4$ nanospheres (Fig. 2e) and the diameter of the nanospheres is only about 100 nm (this is also validated by TEM images in Fig. 3). The small particle size can greatly increase the specific surface area, thus providing more electrochemical reaction sites. Additionally, as illustrated in Fig. 2f–j, the components of nickel, cobalt and sulfur are uniformly distributed in $CNTs/NiCo_2S_4$ composite samples.

The TEM images of pure $NiCo_2S_4$ and $CNTs/NiCo_2S_4$ samples are illustrated in Fig. 3. The diameter of pure $NiCo_2S_4$ nanospheres in Fig. 3a is approximately 400 nm. Meanwhile, it clearly found in Fig. 3d that the $NiCo_2S_4$ particles anchored around the interlocking CNTs displays a smaller diameter of about 100 nm. The interwoven CNTs can form a good electron transport network, and the smaller size of $NiCo_2S_4$ particles is more conducive to electrochemical performance. Fig. 3b and e show the obvious lattice fringes with layer spacing of 0.23, 0.28 and 0.33 nm, respectively, which correspond to the (400), (311) and (440) crystal planes in the $NiCo_2S_4$ structure, respectively. The SAED pattern of the $NiCo_2S_4$ and $CNTs/NiCo_2S_4$ samples in Fig. 3c and f reveal a characteristics of multi-point ring, proving
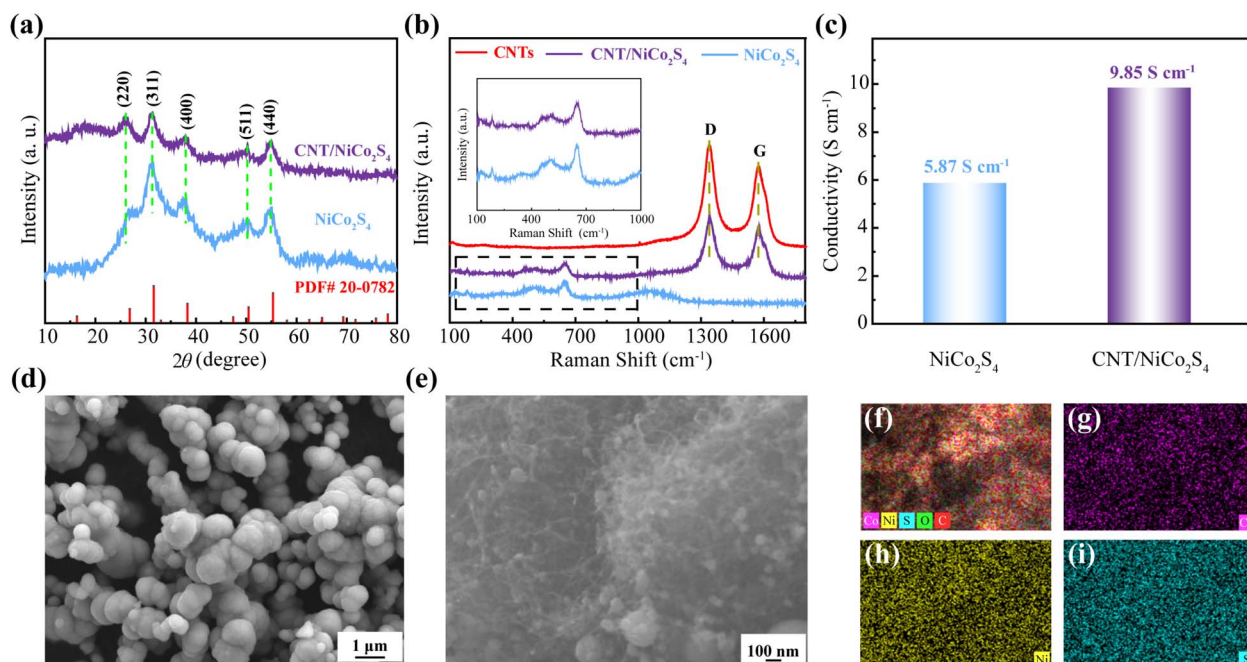
Fig. 2 XRD patterns (a), Raman spectra (b), and bar graph for electrical conductivity (c) of CNTs/NiCo$_2$S$_4$ and NiCo$_2$S$_4$. NiCo$_2$S$_4$ (d) and CNTs/NiCo$_2$S$_4$ (e) SEM images. EDS line scan curve (f) and element mapping pictures for Ni (g), Co (h) and S (i) from a CNTs/NiCo$_2$S$_4$ sample.

polycrystalline structure.[40,41] Moreover, the mapping images of NiCo$_2$S$_4$@CNTs nanocomposite are shown in Fig. 3g–l, which further demonstrates the uniformity of element distribution.

The elemental composition and valence states of the surface from CNTs/NiCo$_2$S$_4$ nanocomposite were examined by XPS technique shown in Fig. 4. The full spectrum is depicted in
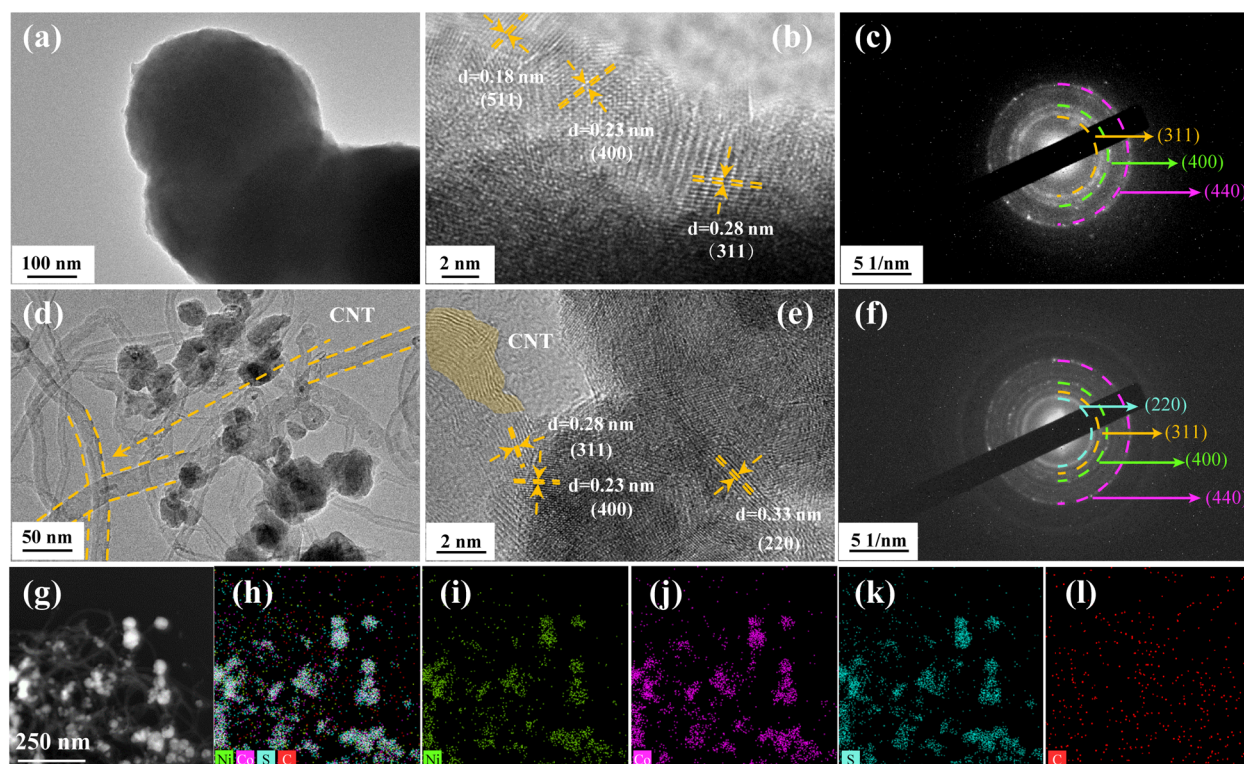

Fig. 3 TEM photographs at low and high magnification of NiCo$_2$S$_4$ and CNTs/NiCo$_2$S$_4$ (a, b, d, e) and the selected-area electron diffraction pattern (c and f). Mapping images of CNTs/NiCo$_2$S$_4$ nanocomposite (g–l).
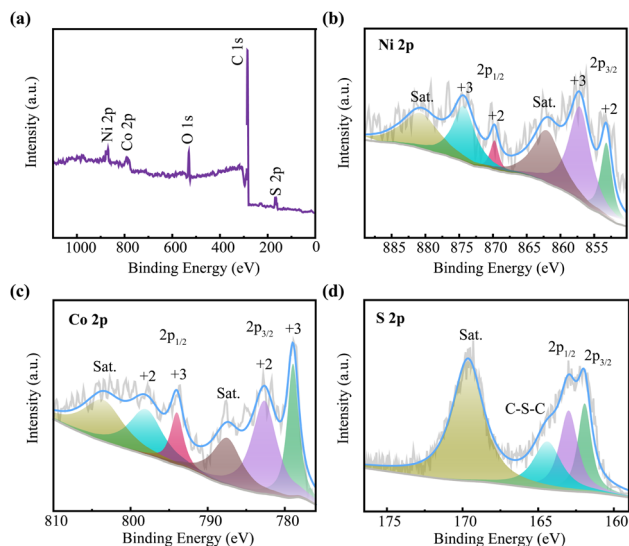
Fig. 4 The total XPS spectrum of CNTs/NiCo$_2$S$_4$ (a) and the corresponding high-resolution spectra of Ni 2p (b), Co 2p (c), and S 2p (d).

Fig. 4a, which displays the Ni, S, Co, and O element signals. Fig. 4b is the fine Ni 2p spectrum and it contains three main peaks, belonging to Ni 2p$_{3/2}$, Ni 2p$_{1/2}$ and shake-up satellite (abbreviated as "sat") respectively. Similarly, Co 2p spectrum in Fig. 4c is divided into three peaks, which are ascribed to Co 2p$_{1/2}$, Co 2p$_{3/2}$ and sat respectively.[42] These results show that Ni (contains Ni^{2+} and Ni^{3+}) and Co (contains Co^{2+} and Co^{3+}) coexist in NiCo$_2$S$_4$ phase. Fig. 4d depicts the S 2p spectrum, which fits three peaks and one dithered satellite peak.[43]

Fig. 5a depicts the GCD curves of NiCo$_2$S$_4$ and CNTs/NiCo$_2$S$_4$ composites. The period of discharge of CNTs/NiCo$_2$S$_4$ is clearly longer than that of neat NiCo$_2$S$_4$, showing that the CNTs/NiCo$_2$S$_4$ electrode has better electrochemical performance than the NiCo$_2$S$_4$ electrode. This is mostly owing to the composite structure established between NiCo$_2$S$_4$ and CNTs, which improves ion transport, in addition to the carbon nanotube network's enhanced electrical conductivity. According to Fig. 5b, the discharge specific capacitance of CNTs/NiCo$_2$S$_4$ can reach 633 C g^{-1} even at a large current density of 30 A g^{-1}. Interestingly, Fig. 5c reveals that CNTs/NiCo$_2$S$_4$ has a larger integral area than NiCo$_2$S$_4$, indicating an improved electrochemical performance. Besides, each GCD curve has good symmetry, which indicates that it has excellent electrochemical reversibility and multiplicity. When scanning speeds differ, the CV curve for CNTs/NiCo$_2$S$_4$ remains reasonably symmetric (Fig. 5d). The EIS diagram of as-prepared NiCo$_2$S$_4$ and CNTs/NiCo$_2$S$_4$ electrodes is presented in Fig. 5e. It was discovered that the EIS of NiCo$_2$S$_4$ and CNTs/NiCo$_2$S$_4$ electrodes are semicircles at high frequencies and oblique lines at low frequencies. Furthermore, the CNTs/NiCo$_2$S$_4$ electrode has a smaller semicircular diameter than NiCo$_2$S$_4$, indicating a lower transfer impedance,[44] which benefit from CNT conductive substrate from composite. As shown in Fig. 5f, the cycle durability of the manufactured CNTs/NiCo$_2$S$_4$ electrode was evaluated in a three-electrode system, where the blue line indicates the capacity of
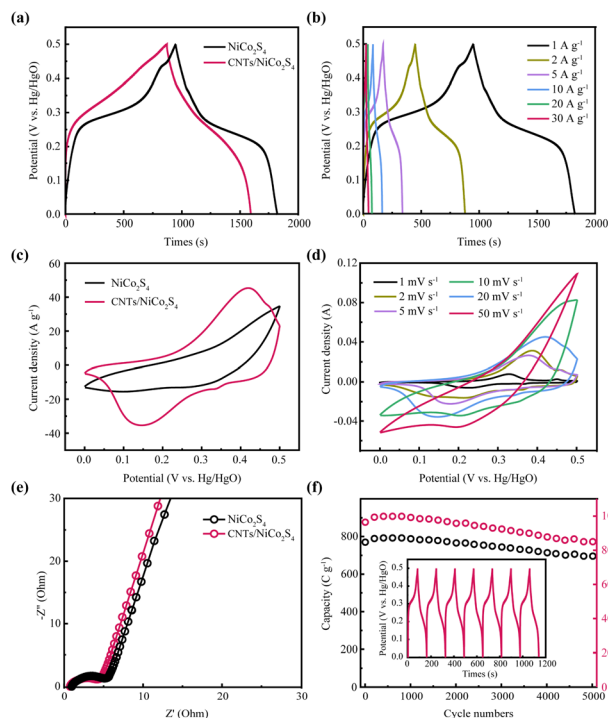

Fig. 5 Galvanostatic charge–discharge curves of NiCo$_2$S$_4$ and CNTs/NiCo$_2$S$_4$ electrodes at 1 A g^{-1} (a). Rate capability of the CNTs/NiCo$_2$S$_4$ electrode tested by galvanostatic charge–discharge technique at various current densities (b). CV curves of NiCo$_2$S$_4$ and CNTs/NiCo$_2$S$_4$ electrodes at a scan rate of 10 mV s^{-1} (c). CV curves of the CNTs/NiCo$_2$S$_4$ electrode at different scan speeds (d). Electrochemical impedance spectroscopy (EIS) spectra of NiCo$_2$S$_4$ and CNTs/NiCo$_2$S$_4$ electrodes (e). Cycle duribility of the CNTs/NiCo$_2$S$_4$ electrode at 10 A g^{-1} (f). Inset of (f) is the partial charge and discharge curves during cycle test.

the electrode material during the whole cycle, while the purple line shows the capacity retention rate. With over 5000 charge–discharge cycles, CNTs/NiCo$_2$S$_4$ electrodes retain capacitance as high as 85%, revealing extraordinary cycling stability.

In this work, an asymmetric supercapacitor was constructed by using CNTs/NiCo$_2$S$_4$ as positive electrode to evaluate the electrochemical property. Fig. 6a displays the CV curves for CNTs/NiCo$_2$S$_4$ and activated carbon (AC). Fig. 6b represents the CV curves of the built supercapacitor at a wide potential window from 0 to 1.6 V. Furthermore, Fig. 6c displays the charge–discharge curves of the fabricated asymmetric supercapacitors at variety of current densities with a high symmetry, showing the outstanding reversibility and superior coulombic efficiency. Additionally, the established supercapacitors have a high specific capacitance of up to 204.8 C g^{-1} at 1 A g^{-1} and the retention ratio is approximately 87% when the current density is up to 20 A g^{-1} as shown in Fig. 6d. Fig. 6e depicts the Ragone diagram for an asymmetric supercapacitor. The assembled asymmetric supercapacitor displays a remarkable energy density of 43.3 W h kg^{-1} under the power density of 800 W kg^{-1}, and the energy density maintains at 31.1 W kg^{-1} when the power density reaches as high as 16 000 W kg^{-1}, confirming the excellent rate capability. Fig. 6f represents the supercapacitor's
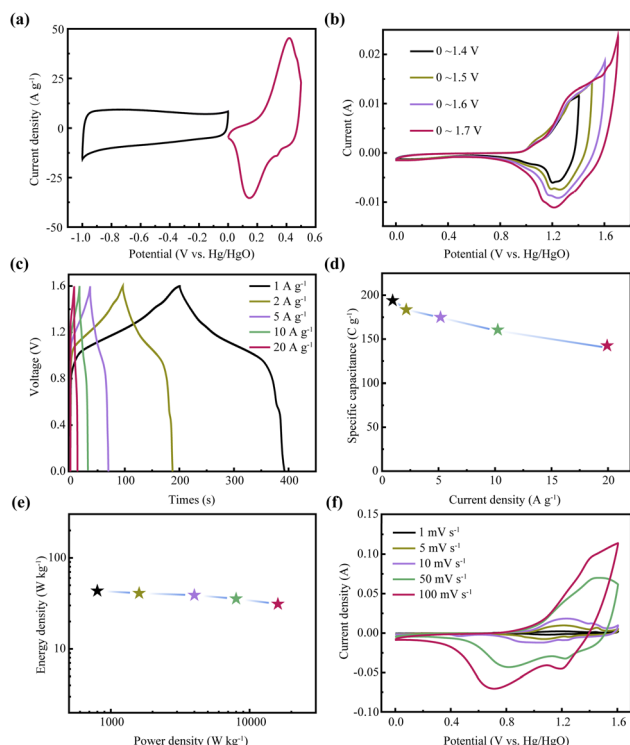
Fig. 6 CV curves of AC and CNTs/NiCo$_2$S$_4$ composite scanned at 10 mV s^{-1} (a). CV curves of CNTs/NiCo$_2$S$_4$-based asymmetric supercapacitor with a scan rate of 10 mV s^{-1} at various potential windows (b), and its charge–discharge curves (c) and specific capacitance (d) at varying current densities. Ragone plot of asymmetric supercapacitor (e). The CV curves of the asymmetric supercapacitor at various scan rates (f).

CV curves, where the redox peak exhibits faradic-type behavior of asymmetric supercapacitor.

4. Conclusions

In summary, we have successfully engineered CNTs/NiCo$_2$S$_4$ nanocomposite by a facile one-step method. CNTs/NiCo$_2$S$_4$ electrode for supercapacitor presents excellent rate performance, outstanding cycle stability (the capacitance retention rate is maintain at 83.5% after 5000 cycles), and a high specific capacitance (890 C g^{-1} at 1 A g^{-1}). Moreover, the CNTs/NiCo$_2$S$_4$-based asymmetric supercapacitor displays a high energy density of 43.3 W h kg^{-1} at a power density of 800 W kg^{-1}. The enhanced capacitive performance can be ascribed to the structural feature of CNTs/NiCo$_2$S$_4$, such as the conductive network generated by carbon nanotubes, the size reduction of NiCo$_2$S$_4$, and their synergistic impact. Therefore, the technique adopted in this work provide a great guidance to proceed to the construction of battery-supercapacitor electrode materials.

Author contributions

Junming Chen: resources, writing – review & editing, methodology. Zhiling Du: writing – review & editing, methodology. Kun Cheng: resources, visualization. Jusheng Bao: visualization, writing – review & editing. Guiling Wang: investigation, visualization. Yue Yao: resources. Jiayi Song: resources. Jing Yue: resources. Kun Xu: resources. Weicheng Xie: resources. Wei Qiang: resources. You Liu: formal analysis, visualization, resources, writing – original draft. Xuchun Wang: funding acquisition, project administration, supervision.

Conflicts of interest

There are no conflicts to declare.

Acknowledgements

References

1 L. Hou, Y. Shi, S. Zhu, M. Rehan, G. Pang, X. Zhang and C. Yuan, *J. Mater. Chem. A*, 2017, **5**, 133–144.

2 L. Yang, X. Lu, S. Wang, J. Wang, X. Guan, X. Guan and G. Wang, *Nanoscale*, 2020, **12**, 1921–1938.

3 X. Yang, X. He, Q. Li, J. Sun, Z. Lei and Z.-H. Liu, *Energy Fuels*, 2021, **35**, 3449–3458.

4 Y. Gao, B. Wu, J. Hei, D. Gao, X. Xu, Z. Wei and H. Wu, *Electrochim. Acta*, 2020, **347**, 136314.

5 Y. Chang, H. Shi, X. Yan, G. Zhang and L. Chen, *Carbon*, 2020, **170**, 127–136.

6 J. Castro-Gutiérrez, A. Celzard and V. Fierro, *Front. Mater.*, 2020, **7**, 1–25.

7 R. Teymourfar, B. Asaei, H. Iman-Eini and R. Nejati fard, *Energy Convers. Manage.*, 2012, **56**, 206–214.

8 A. T. Hamada and M. F. Orhan, *J. Energy Storage*, 2022, **52**, 105033.

9 T. Bi, J. Jiang, Y. Lei, X. Zheng, Z. Jia, Z. Wei and H. Yang, *Appl. Surf. Sci.*, 2020, **530**, 147317.

10 Bharti, A. Kumar, G. Ahmed, M. Gupta, P. Bocchetta, R. Adalati, R. Chandra and Y. Kumar, *Nano Express*, 2021, **2**, 022004.

11 S. Balasubramaniam, A. Mohanty, S. K. Balasingam, S. J. Kim and A. Ramadoss, *Nano-Micro Lett.*, 2020, **12**, 85.

12 L. L. Zhang and X. S. Zhao, *Chem. Soc. Rev.*, 2009, **38**, 2520–2531.

13 Q. Dou and H. S. Park, *Energy Environ. Mater.*, 2020, **3**, 286–305.

14 P. K. Panda, A. Grigoriev, Y. K. Mishra and R. Ahuja, *Nanoscale Adv.*, 2020, **2**, 70–108.

15 H. Li, W. Zhang, Z. Han, K. Sun, C. Gao, K. Cheng, Z. Liu, Q. Chen, J. Zhang, Y. Lai, Z. Zhang and H. Sun, *Mater. Today Energy*, 2021, **21**, 100754.

16 T. Liu and Y. Li, *InfoMat*, 2020, **2**, 807–842.

17 P. Selinis and F. Farmakis, *J. Electrochem. Soc.*, 2022, **169**, 010526.

18 J. Dong, S. Li and Y. Ding, *J. Alloys Compd.*, 2020, **845**, 155701.

19 W. Peng, H. Chen, W. Wang, Y. Huang and G. Han, *Curr. Appl. Phys.*, 2020, **20**, 304–309.

20 M. Barazandeh and S. H. Kazemi, *Sci. Rep.*, 2022, **12**, 4628.

21 Y. Song, Q. Pan, H. Lv, D. Yang, Z. Qin, M.-Y. Zhang, X. Sun and X.-X. Liu, *Angew. Chem., Int. Ed.*, 2021, **60**, 5718–5722.

22 J. Meng, Y. Song, Z. Qin, Z. Wang, X. Mu, J. Wang and X.-X. Liu, *Adv. Funct. Mater.*, 2022, **32**, 2204026.

23 Z. Ma, L. Fan, F. Jing, J. Zhao, Z. Liu, Q. Li, J. Li, Y. Fan, H. Dong, X. Qin and G. Shao, *ACS Appl. Energy Mater.*, 2021, **4**, 3983–3992.

24 R. Bian, D. Song, W. Si, T. Zhang, Y. Zhang, P. Lu, F. Hou and J. Liang, *ChemElectroChem*, 2020, **7**, 3663–3669.

25 X. Rui, H. Tan and Q. Yan, *Nanoscale*, 2014, **6**, 9889–9924.

26 Y. Wang, Z. Chen, T. Lei, Y. Ai, Z. Peng, X. Yan, H. Li, J. Zhang, Z. M. Wang and Y.-L. Chueh, *Adv. Energy Mater.*, 2018, **8**, 1703453.

27 X. Wang, Y. Deng, Z. Wang, Z. Li, L. Wang, J. Ouyang, C. Zhou and Y. Luo, *ACS Appl. Energy Mater.*, 2022, **5**, 7400–7407.

28 J. Qi, H. Gu, C. Ruan, L. Zhu, Q. Meng, Y. Sui, X. Feng, W. Wei and H. Zhang, *Ionics*, 2022, **28**, 2979–2989.

29 P. Phonsuksawang, P. Khajondetchairit, K. Ngamchuea, T. Butburee, S. Sattayaporn, N. Chanlek, S. Suthirakun and T. Siritanon, *Electrochim. Acta*, 2021, **368**, 137634.

30 F. Ren, Y. Ji, S. Tan and F. Chen, *Inorg. Chem. Front.*, 2021, **8**, 72–78.

31 G. Xue, T. Bai, W. Wang, S. Wang and M. Ye, *J. Mater. Chem. A*, 2022, **10**, 8087–8106.

32 H. Wang and X. Wang, *ACS Appl. Mater. Interfaces*, 2013, **5**, 6255–6260.

33 K. Cao, L. Jiao, H. Xu, H. Liu, H. Kang, Y. Zhao, Y. Liu, Y. Wang and H. Yuan, *Adv. Sci.*, 2016, **3**, 1500185.

34 Z. Sun, Y. Zhao, C. Sun, Q. Ni, C. Wang and H. Jin, *Chem. Eng. J.*, 2022, **431**, 133448.

35 Y. Huang, M. Cheng, Z. Xiang and Y. Cui, *R. Soc. Open Sci.*, 2018, **5**, 180953.

36 M. Sajjad, X. Chen, C. Yu, L. Guan, S. Zhang, Y. Ren, X. Zhou and Z. Liu, *J. Mol. Eng. Mater.*, 2019, **7**, 1950004.

37 Y. Luan, H. Zhang, F. Yang, J. Yan, K. Zhu, K. Ye, G. Wang, K. Cheng and D. Cao, *Appl. Surf. Sci.*, 2018, **447**, 165–172.

38 Z. Sun, C. Zhao, X. Cao, K. Zeng, Z. Ma, Y. Hu, J.-H. Tian and R. Yang, *Electrochim. Acta*, 2020, **338**, 135900.

39 Y. Gao, Q. Lin, G. Zhong, Y. Fu and X. Ma, *J. Alloys Compd.*, 2017, **704**, 70–78.

40 J. Zou, D. Xie, F. Zhao, H. Wu, Y. Niu, Z. Li, Q. Zou, F. Deng, Q. Zhang and X. Zeng, *J. Mater. Sci.*, 2021, **56**, 1561–1576.

41 F. Yu, Z. Chang, X. Yuan, F. Wang, Y. Zhu, L. Fu, Y. Chen, H. Wang, Y. Wu and W. Li, *J. Mater. Chem. A*, 2018, **6**, 5856–5861.

42 G. Xiang, Y. Meng, G. Qu, J. Yin, B. Teng, Q. Wei and X. Xu, *Sci. Bull.*, 2020, **65**, 443–451.

43 Y. Meng, P. Sun, W. He, B. Teng and X. Xu, *Nanoscale*, 2019, **11**, 688–697.

44 M. Chuai, K. Zhang, X. Chen, Y. Tong, H. Zhang and M. Zhang, *Chem. Eng. J.*, 2020, **381**, 122682.